

Surface photoeffect for metals: Energy and angular electron distributions*

K. L. Kliewer

Ames Laboratory-ERDA and Department of Physics, Iowa State University, Ames, Iowa 50011

(Received 7 September 1976)

The nonlocal theory of the author for the surface photoeffect produced in metals by p -polarized light is used to obtain energy and angular electron distributions for a range of low to moderate excitation energies. Considering only the effects from single-particle excitations, the energy distribution curves have, in general, a roughly triangular shape with the peak occurring for initial states near the Fermi energy. There is also a high-energy tail due to damping. Features in the angular distribution curves include confinement to decreasing angles with increasing light frequency and low-angle structure resulting from damping. Very striking structure appears in the energy-resolved angular distributions when the light frequency ω is such that $\hbar\omega > E_F + \Phi$, where E_F is the Fermi energy and Φ the work function. A number of significant changes, including a sharp increase in the total yield, occur in the various distributions when Landau damping sets in, that is, when the plasmon enters the single-particle-excitation region. Arguments are presented that there is no reason to expect that the nonlocal surface contributions to the yield should vanish above the plasma frequency.

I. INTRODUCTION

Several photoemission theories based on a nonlocal description of the optical absorption have appeared recently.¹⁻³ The need for such a description arises from the fact that the electric field in the surface region of a metal subjected to optical illumination is markedly different from that given by a local description. Since the escape length for photoelectrons is short, a proper analysis of photoemission requires a careful treatment of the surface-region field. Results available to this time, both theoretical¹⁻⁴ and experimental,^{4,5} indicate that the nonlocal effects are of major importance for photoemission resulting from low or moderate excitation energies.

Nonlocal photoemission theories to this time have dealt primarily with p -polarized excitation. The reason for this is that such light has an electric field component normal to the surface, which is associated with particularly prominent and unique nonlocal effects of longitudinal character. It has been argued² that these longitudinal effects are a prime cause of the singular effectiveness of p -polarized light in producing photoelectrons.

The incorporation of nonlocal effects imparts a striking spatial dependence to the electric field near the surface. In the nonlocal theory of the author,^{1,2} attention was drawn to the consequent oscillatory character of the spatial distribution of the absorbed energy. It was shown that these oscillations result from plasmons and single-particle excitations; which type of excitation is dominant depends on the light frequency. In Sec. II of this paper, we expand on our previous work by demonstrating the quantitative connection between the spatial distribution of the absorbed energy and the elementary excitation spectrum.

This spectrum is then converted to energy and angular photoelectron distributions using the three-step photoemission model. However, the escape length is essentially irrelevant for the surface process of interest here. Again, attention is focused on effects associated with the electric field component normal to the surface. Results for a wide range of light frequencies are presented and discussed in Sec. III; included here is a discussion of the photoemission role of the plasmon. Conclusions are given in Sec. IV.

II. EXCITATION SPECTRUM AND THE PHOTOELECTRON DISTRIBUTIONS

The starting point for the present discussion is given in Ref. 2; essential elements will be reviewed here very briefly. We take as a model for the metallic photoemitter an electron gas filling the half space $z > 0$, with the region $z < 0$ vacuum. The surface of the electron gas is assumed to scatter the internal electrons specularly. P -polarized light of angular frequency ω is incident upon the photoemitter in the x - z plane at angle θ , measured from the surface normal. With A , the absorptance of the metal, the distribution of absorbed energy

$$\frac{dA}{dz} \propto \text{Re}[\vec{J}(z) \cdot \vec{E}^*(z)],$$

where $\vec{J}(z)$ is the z -dependent part of the current resulting from the electric field $\vec{E}(z)$ within the photoemitter. We calculate both \vec{J} and \vec{E} nonlocally thereby obtaining the nonlocal dA/dz . Although dA/dz includes two terms, $\text{Re}[J_x(z)E_x^*(z)]$ and $\text{Re}[J_z(z)E_z^*(z)]$, we will here concern ourselves largely with the latter. Indeed, unless otherwise stated, when we speak below of dA/dz we will

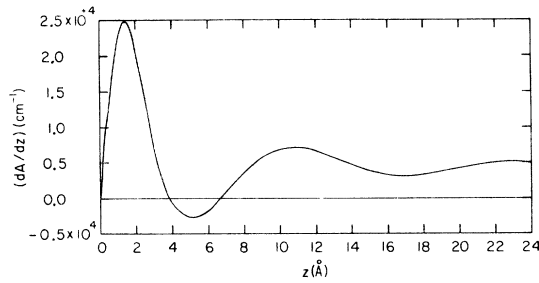


FIG. 1. Distribution of absorbed energy dA/dz for $\Omega=0.75$, $\gamma=10^{-2}$, and $\theta_I=45^\circ$.

be referring to the contribution from the z components. In so doing, we are not implying that the contribution from the x components is of no consequence. Rather, our interest here is in effects peculiar to p -polarized light and, thus, effects associated with the normal component of the electric field.

Calculations have been made with the electron gas density that of sodium. This means a Fermi velocity $v_F=1.07 \times 10^8$ cm/sec, a Fermi energy $E_F=3.26$ eV, and a plasma frequency ω_p such that $\hbar\omega_p=6.07$ eV. We define $\Omega=\omega/\omega_p$ and use as a measure of damping $\gamma=(\omega_p \tau)^{-1}$, where τ is the mean electron lifetime.

To provide a specific example for the presentation of the basic theory, we have chosen the conditions $\Omega=0.75$, $\gamma=10^{-2}$, and $\theta_I=45^\circ$. The spatial dependence of dA/dz for these conditions is shown

in Fig. 1. (Keep in mind that this dA/dz includes only the contribution from the z components of \vec{J} and \vec{E} .) For comparison we give in Table I the values of dA/dz [there denoted $(dA/dz)_z$] at $z=0$ and $z=24 \text{ \AA}$, the absorption coefficient α , and the contribution from the x components $(dA/dz)_x$, all for the case where the calculation is local. From these numbers and Fig. 1, it is apparent that the nonlocal value of dA/dz differs from the local for $z \lesssim 30 \text{ \AA}$, and differs markedly for small z . As discussed in Ref. 2, these oscillations, or standing absorption waves, result from interference between elementary excitations moving toward and away from the surface. Since we are here below the plasma frequency, the elementary excitations are the single-particle excitations.

The question we then ask is, what is the spectrum of excited electrons which gives rise to this dA/dz ? To answer this question, we must remember that the nonlocal field can transfer the large momenta represented by the oscillations in Fig. 1 only in the direction normal to the surface, that is, in the $\pm z$ directions. This momentum will be represented by the wave vector in the z direction, designated q . We then define the Fourier transform A_q of dA/dz by

$$\frac{dA}{dz} = \int_{-\infty}^{\infty} dq A_q e^{iqz}. \quad (2.1)$$

Because dA/dz is rigorously equal to zero at

TABLE I. Parameters characterizing the distribution of absorbed energy in the local approximation. The total dA/dz is $\alpha A e^{-\alpha z}$, where α is the absorption coefficient given by Eq. (2.6) and A is the total local absorptance. Associated with the z component of the electric field, the distribution of absorbed energy is $(dA/dz)_z = \alpha A_z e^{-\alpha z}$, and with the x component $(dA/dz)_x = \alpha A_x e^{-\alpha z}$. A_z is given by Eq. (3.4) and $A_x = 4\Omega\omega_p \epsilon'' \cos\theta_I |\epsilon - \sin^2\theta_I| / \alpha c |\epsilon \cos\theta_I + (\epsilon - \sin^2\theta_I)^{1/2}|^2$, with the local dielectric function $\epsilon = \epsilon' + i\epsilon''$. The total absorptance $A = A_x + A_z$. All values are in $(\text{cm})^{-1}$.

Ω	γ	θ_I (in deg.)	α	$\left(\frac{dA}{dz}\right)_z \Big _{z=0}$	$\left(\frac{dA}{dz}\right)_z \Big _{z=24 \text{ \AA}}$	$\left(\frac{dA}{dz}\right)_x \Big _{z=0}$
0.75	10^{-2}	45	5.22×10^5	4.81×10^3	4.25×10^3	1.23×10^4
0.99	10^{-2}	45	4.39×10^5	8.36×10^3	7.53×10^3	8.70×10^3
0.99	10^{-4}	45	4.39×10^5	8.53×10^1	7.67×10^1	8.88×10^1
0.999	10^{-4}	45	4.36×10^5	8.68×10^1	7.82×10^1	8.72×10^1
1.20	10^{-2}	45	3.26×10^5	1.22×10^4	1.13×10^4	4.75×10^3
1.50	10^{-2}	45	5.80×10^3	4.89×10^3	4.88×10^3	5.45×10^2
1.50	10^{-1}	75	5.66×10^5	3.18×10^4	2.78×10^4	1.28×10^4
1.50	10^{-2}	75	5.67×10^5	3.30×10^3	2.88×10^3	1.34×10^3
1.50	10^{-3}	75	5.67×10^5	3.32×10^2	2.90×10^2	1.34×10^2
1.60	10^{-1}	75	5.59×10^5	3.20×10^4	2.80×10^4	1.11×10^4
1.60	10^{-3}	75	5.60×10^5	3.33×10^2	2.91×10^2	1.16×10^2
2.00	10^{-2}	45	1.54×10^3	1.02×10^3	1.02×10^3	5.12×10^2
2.00	10^{-2}	75	5.27×10^5	3.35×10^3	2.95×10^3	6.58×10^2
2.50	10^{-2}	60	1.64×10^3	1.42×10^3	1.42×10^3	1.71×10^2
2.50	10^{-2}	75	4.69×10^5	3.38×10^3	3.02×10^3	3.37×10^2
3.00	10^{-2}	67	1.68×10^3	1.49×10^3	1.49×10^3	7.31×10^1
3.00	10^{-2}	75	3.88×10^5	3.39×10^3	3.09×10^3	1.60×10^2

$z=0$ for the electron gas,² and because of the field symmetries for our specular scattering model,² we take

$$\left. \frac{dA}{dz} \right|_{-z} = - \left. \frac{dA}{dz} \right|_z.$$

Then

$$\begin{aligned} A_q &= \frac{1}{2\pi} \int_{-\infty}^{\infty} \left(\frac{dA}{dz} \right) e^{-iqz} dz \\ &= -\frac{i}{\pi} \int_0^{\infty} \left(\frac{dA}{dz} \right) \sin(qz) dz \\ &\equiv -iA'_q \end{aligned} \quad (2.2)$$

and $A_{-q} = -A_q$, $A'_{-q} = -A'_q$. For use below, we note that the absorptance $A = \int_0^{\infty} (dA/dz) dz$ (remember that this is only that part due to the z components of \vec{J} and \vec{E}) is given also by

$$A = 2i \int_0^{\infty} \frac{A_q}{q} dq = 2 \int_0^{\infty} \frac{A'_q dq}{q}. \quad (2.3)$$

From this equation it is clear that the transform of importance is A'_q and A'_q for dA/dz of Fig. 1 is given in Fig. 2 as a function of $Q = qc/\omega_p$.

To appreciate the content of Fig. 2, we note that the single-particle excitation region for fixed ω (calculated with no damping) extends from the small- q parabola (denoted lo- q)

$$q_{\text{lo-}q} = -k_F + (k_F^2 + 2m\omega/\hbar)^{1/2}, \quad (2.4)$$

with k_F the magnitude of the Fermi wave vector and m the electron mass, to the large- q parabola (denoted hi- q)

$$q_{\text{hi-}q} = k_F + (k_F^2 + 2m\omega/\hbar)^{1/2}. \quad (2.5)$$

For the conditions of Fig. 2, $Q_{\text{lo-}q} = q_{\text{lo-}q}c/\omega_p = 164.8$ and $Q_{\text{hi-}q} = q_{\text{hi-}q}c/\omega_p = 766.0$ as indicated in the figure. Thus, our previous statement that the oscillations in dA/dz result from single-particle oscillations is clearly established and it is the region of q space near the low- q edge which contributes most significantly to the oscillations, a

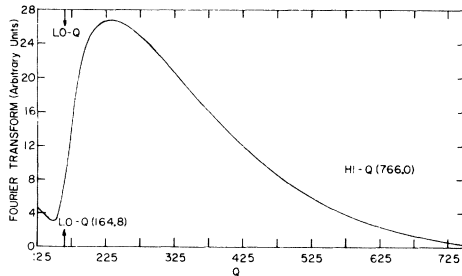


FIG. 2. Fourier transform A'_q of dA/dz for $\Omega = 0.75$, $\gamma = 10^{-2}$, and $\theta_I = 45^\circ$. The dimensionless wave vector $Q = qc/\omega_p$, with c the speed of light and q the wave vector in the z direction.

point noted and discussed previously.²

In Fig. 2, A'_q reaches a minimum somewhat below the low- q edge, and then increases, as q decreases further, to a maximum near $q=0$ (at $q=0, A'_q=0$). Our calculation of dA/dz included a finite electron lifetime and, thus, a local or Drude absorption contribution. This is apparent from Fig. 1 and Table I where we see that the oscillations for $z \geq 10 \text{ \AA}$ occur about the local value of dA/dz , which is proportional to $e^{-\alpha z}$, where the classical absorption coefficient α is given by

$$\alpha = (2\omega/c) \text{Im}[\epsilon(\omega) - \sin^2\theta_I]^{1/2} \quad (2.6)$$

and $\epsilon(\omega)$, the local dielectric function, by

$$\epsilon = 1 - [\Omega(\Omega + i\gamma)]^{-1}. \quad (2.7)$$

That this local part of dA/dz includes contributions from large q values, even though usually thought of as a $q \sim 0$ effect, can be shown as follows. The nonlocal surface impedance for the electron gas model employed here is⁶

$$\begin{aligned} Z_p &= \frac{2i\omega}{\pi c} \int_0^{\infty} \frac{dq}{q_T^2} \\ &\times \left(\frac{\sin^2\theta_I}{\epsilon_l(q_T, \omega)} + \frac{q^2}{(\omega^2/c^2)\epsilon_t(q_T, \omega) - q_T^2} \right), \end{aligned} \quad (2.8)$$

where ϵ_l and ϵ_t are the nonlocal longitudinal and transverse dielectric functions and $q_T = (q^2 + q_x^2)^{1/2}$ with $q_x = \omega \sin\theta_I/c$. The total absorptance for the system goes roughly like $\text{Re}(Z_p)$. In the local approximation, this expression for Z_p is modified by making the following replacements:

$$\epsilon_l(q_T, \omega) \rightarrow \lim_{q_T \rightarrow 0} \epsilon_l(q_T, \omega) = \epsilon(\omega)$$

and

$$\epsilon_t(q_T, \omega) \rightarrow \lim_{q_T \rightarrow 0} \epsilon_t(q_T, \omega) = \epsilon(\omega).$$

Thus

$$Z_p|_{\text{local}} = \frac{2i\omega}{\pi c} \int_0^{\infty} \frac{dq}{q_T^2} \left(\frac{\sin^2\theta_I}{\epsilon(\omega)} + \frac{q^2}{(\omega^2/c^2)\epsilon(\omega) - q_T^2} \right).$$

Since $q_x = (\omega/c) \sin\theta_I$ is small, we see that in the local case the absorptance includes large- q contributions going like $1/q^2$. It is this local contribution which causes A'_q in Fig. 2 to bend up again below the low- q edge of the single-particle region. It should be noted that the local contribution to A'_q does not drop off as rapidly as $1/q^2$. The argument just given indicates that the local contribution to the absorptance goes as $1/q^2$. From Eq. (2.3), this means that A'_q should drop off as $1/q$ and this is indeed the case for q below

the low- q single-particle edge and not too near zero, that is, $q_s < q < q_{10-q}$.

The q_T^{-2} factor appearing outside the large parentheses in Eq. (2.8), resulting from the Fourier transform of the Coulomb interaction, has an additional effect. It clearly favors excitations of smaller q and is to a large extent responsible for the fact that A'_q in Fig. 2 is large only near the low- q edge of the single-particle region.

In addition to generating local effects in the absorptance and thus in A'_q , the inclusion of a finite electron lifetime spreads the edges of the single-particle-excitation region. This is indicated in Fig. 2 by the fact that A'_q has a substantial value at the low- q edge which was determined above assuming no damping. If there were no damping, A'_q would be zero at the edge. This spread has interesting effects, as we will see below, and is the principal manifestation of damping in the realm of single-particle, nonlocal effects. However, and we emphasize this point, the basic single-particle, nonlocal character is affected only to a modest extent by damping. That is, the oscillations of Fig. 1, although superposed upon a background which is strongly dependent upon the damping, are themselves only weakly dependent.

An additional demonstration that the damped oscillations of Fig. 1 result from interference between standing waves with a spread of q values can be given using standard wave properties. Since $\Delta q \Delta z \sim 1$, we find from Fig. 2 that $\Delta Q \sim 200$, so $\Delta q \sim 6 \times 10^7 \text{ cm}^{-1}$, and thus $\Delta z \sim 2 \text{ \AA}$. Recognizing that we are here dealing with Δ values determined at points which are roughly half maximum, this result is indeed consistent with Fig. 1.

Our task now is to convert the distribution represented by Fig. 2 into a photoyield, to which only electrons moving toward the surface contribute. The usual procedure is to introduce an escape length ξ for the electrons at this point. Let us do so also and then comment immediately below on the significance of ξ . The internal photoyield Y' , that is, the yield of electrons reaching the surface, is

$$Y' = \int_0^\infty dz e^{-z/\xi} \text{Re} \left(\frac{dA}{dz} \Big|_{q < 0} \right) = \int_0^\infty dq \frac{A'_q q}{\xi^{-2} + q^2}. \tag{2.9}$$

As $\xi \rightarrow \infty$, Y' is just half the absorptance [see Eq. (2.3)], as expected, since only half of the absorbed energy is associated with electrons moving toward the surface.

If we think of the wave vector q in Eq. (2.9) as complex due to finite lifetime effects, $q = q_1 + iq_2$,

the role of ξ is just that of q_2 . In an analysis where the uncertainty in momentum transfer associated with the finite lifetime is properly included, the physical effects represented by the introduction of ξ would appear automatically. For the nonlocally excited electrons, ξ is essentially irrelevant. The q values for these electrons are such that $q\xi > 1$ for $\xi \gtrsim 2 \text{ \AA}$ so for all but the smallest escape lengths, ξ can be taken to be infinite in Eq. (2.9), that is, Y' is independent of ξ . This indicates that the nonlocal yield is a genuine surface effect and is so because the nonlocally excited electrons are concentrated near the surface.

To avoid a plethora of negative signs in the next series of arguments, we reverse z so $+z$ is toward the surface. Electrons moving toward the surface are then associated with positive values of the wave vector in the z direction. We also consider henceforth only nonlocal contributions to the yield.

For simplicity, we take the damping to be zero for the moment. In Fig. 3(b) is sketched the excitation spectrum of the electron gas and in Fig. 3(a) the Fermi sphere which represents the initial states of the excited electrons. For a fixed excitation frequency ω (denoted ω' in Fig. 3 and such that $\hbar\omega > E_F$ for reasons which will be clear below) the low- q edge of the single particle region, point P_1 in Fig. 3(b), corresponds to point P_1 on the Fermi sphere in Fig. 3(a). Similarly, the large- q edge of the single-particle region, point P_2 in Fig. 3(b), corresponds to the point P_2 on the

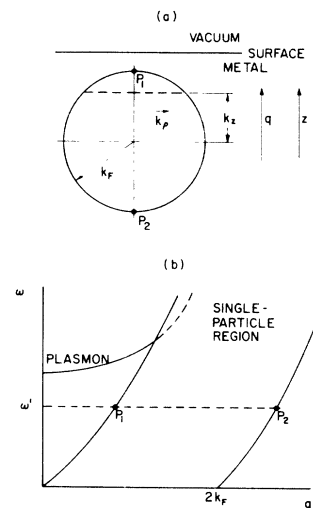


FIG. 3. (a) Initial states for the electron gas with the notation to be used indicated. The wave vector q points toward the surface. (b) Excitation spectrum ω vs q for the electron gas. Points P_1 in the two parts of the figure are equivalent as are points P_2 .

Fermi surface. This can be seen from the standard excitation expression

$$\hbar\omega = (\hbar^2/2m)(\bar{k}_f^2 - \bar{k}_i^2), \quad (2.10)$$

where \bar{k}_f and \bar{k}_i represent, respectively, a final state outside the Fermi surface and an initial state within. With q in the z direction and $\bar{k}_f = \bar{k}_i + q\hat{z}$, \hat{z} a unit vector directed toward the surface,

$$\hbar\omega = (\hbar^2/m)k_z q + (\hbar^2/2m)q^2, \quad (2.11)$$

where k_z is the z component of \bar{k}_i . When $k_z = k_F$, $q = q_{lo-q}$ of Eq. (2.4); when $k_z = -k_F$, $q = q_{hi-q}$ of Eq. (2.5). As we progress from P_1 to P_2 in Fig. 3(b), we move through the Fermi sphere in Fig. 3(a). Each slab of initial state electrons described by a given k_z is then associated with a unique value of q along the line P_1 - P_2 in Fig. 3(b). This means that the value of A'_q of Fig. 2, in the single-particle region, describes the extent of the optical excitation of that slab of electrons with k_z given by (2.11) and such that the excited electrons are moving in the $+z$ direction. The contribution of this slab of electrons to the internal photoyield Y' is, from Eq. (2.9), $A'_q q / (\xi^{-2} + q^2)$.

To find the energy distribution of Y' , we note that the density of electron states per unit energy interval in a plane of fixed k_z , dn/dE , is a constant which we call K . ($K = m/\pi\hbar^2$ but its value is unimportant here.) The number of initial-state electrons in such a plane N_q is then

$$N_q = K[E_F - E_{\min}(q)], \quad (2.12)$$

where

$$E_{\min}(q) = \hbar^2 k_z^2 / 2m. \quad (2.13)$$

Since all of these electrons will have equal probability of excitation under the influence of the z -directed electric field being considered here,

$$\epsilon_i(q, \omega, \tau) = 1 + \frac{[1 + (i/\omega\tau)][\epsilon_i^0(q, \omega + i/\tau) - 1]}{1 + (i/\omega\tau)[\epsilon_i^0(q, \omega + i/\tau) - 1]/[\epsilon_i^0(q, 0) - 1]}, \quad (2.15)$$

with ϵ_i^0 the original Lindhard function. As $\omega \rightarrow 0$, $\epsilon_i(q, \omega, \tau) \rightarrow \epsilon_i^0(q, 0)$, which is just the function obtained if we let $\tau \rightarrow \infty$ in (2.15) before taking the $\omega \rightarrow 0$ limit. Thus $\tau_{\text{eff}}(\omega) \rightarrow \infty$ as $\omega \rightarrow 0$ and there is no energy spread. Since we want to refer our broadened excited-state spectrum back to the sharp initial states through real values of q and ω , we must modify the initial state description from that of the simple Fermi sphere. This is, in fact, what the spread of the single-particle region in Fig. 2 indicates. We emphasize again that the apparent distortion of the initial-state spectrum reflects final-state effects.

that is, all have the same matrix element, we can rewrite Y' as

$$Y' = \int_{q_{lo-q}}^{q_{hi-q}} dq A'_q \frac{q}{\xi^{-2} + q^2} \int_{E_{\min}(q)}^{E_F} \frac{dE}{E_F - E_{\min}(q)}, \quad (2.14)$$

where we have written Y' in terms of initial states. To find Y' in terms of final states, we need only let $E \rightarrow E + \hbar\omega$. The contribution to dY'/dE from a given value of q is constant for E between E_{\min} and E_F , and zero otherwise. The total dY'/dE is just a sum over a group of such rectangular contributions.

Inclusion of damping complicates this picture considerably. As mentioned above, the boundaries of the single-particle region spread outward since each of the excited single-particle states has a finite width. As a result the range of q values in the q integral of Eq. (2.14) expands. In addition, since the single-particle region spreads while the number of electrons is fixed, the energy denominators in Y' of (2.14) must also change. We thus must quantify these effects.

The nonlocal effects we are here considering are due almost entirely to the longitudinal field and, hence, characterized by the longitudinal dielectric function ϵ_l . By inserting a finite lifetime τ into ϵ_l , the resulting excitations of frequency ω will be characterized by an effective lifetime $\tau_{\text{eff}}(\omega)$ and these states will have an energy spread ΔE such that $(\Delta E)\tau_{\text{eff}} \sim \hbar$. In our simple electron gas model the energy of a state of wave vector k is of course $E = \hbar^2 k^2 / 2m$ so $\Delta E = \hbar k \Delta k / m$. A spread in energy is coupled to a spread in momentum. Is this inconsistent with the filled and sharp Fermi sphere we used as our initial-state configuration? Interestingly, the answer is no. The dielectric function which describes the longitudinal response of the system is ⁷

To describe this distortion we note that

$$\lim_{\tau \rightarrow \infty} \text{Im} \epsilon_l^0 = \left(\frac{3\omega_p^2}{q^2 v_F^2} \right) \left(\frac{\pi k_F}{4q} \right) \left[1 - \left(\frac{\omega}{qv_F} - \frac{q}{2k_F} \right)^2 \right]. \quad (2.16)$$

Using Eqs. (2.11) and (2.13), the factor in the parentheses is just $[E_F - E_{\min}(q)]/E_F$, indicating that this factor for given q is proportional to the area of the slab of electrons associated with that z , that is, proportional to the number of electrons in the slab. This suggests the following procedure for finding the energy denominators in Eq. (2.14)

when there is modest damping. Evaluate ϵ_i^0 with damping by letting $\omega \rightarrow \omega + i\omega_p \gamma$. The energy denominator E_{den} will then be

$$E_{\text{den}} = \text{Im}[\epsilon_i^0(q, \omega + i\omega_p \gamma)] E_F / (3\omega_p^2 / q^2 v_F^2) (\pi k_F / 4q), \quad (2.17)$$

and this does indeed describe the “spread” single-particle region seen in Fig. 2. Having now a prescription for finding the total number of electrons in a slab of given k_x , we have to describe how these electrons are distributed in transverse momentum. This we do simply by saying that the density of electrons in a slab of given k_x is the same as without damping over the energy range from E_{min} to $E_{\text{den}} + E_{\text{min}}$, thereby defining a q -dependent effective Fermi energy $E'(q) = E_{\text{den}}(q) + E_{\text{min}}(q)$. The energy integral in Eq. (2.14) will then extend from E_{min} to E' . This procedure gives rise to less electron spreading than actually occurs as we have eliminated the tails of the spread states. It represents, in some sense, a one-dimensional damping. What we have done is move electrons around in the k_x direction (the only direction in which momentum transfer occurs) without adding any broadening in the directions perpendicular to k_x . Our Fermi sphere has become a “Fermi lemon.” The consequences of our model will be very apparent below and the conclusions drawn therefrom can be modified to reflect a better physical description.

Having now a model for the energy distribution, the remaining question relating to damping is, what is the appropriate range of integration for q ? From Fig. 2, it is clear that there is not a unique delineation between the local $\sim 1/q$ tail and the nonlocal region. Our procedure is to integrate from the q value q_1 , corresponding roughly to the minimum in the Fourier transform A'_q , to $q_{\text{hi}-q}$. The large- q part of the single-particle region contributes so little to the yield that the result is insensitive to the exact value of the upper limit. Perhaps a preferable procedure would be to subtract a roughly $1/q$ local contribution from A'_q and call the remainder the nonlocal part. However, a natural question arises: How can a “local” electron in the single-particle region tell it is not a “nonlocal” electron? Thus, we feel justified in our approach. The effect of this procedure will be apparent below and further comments relating to damping will be made then.

Our final expression for the yield Y' including damping then is

$$Y' = \int_{q_1}^{q_{\text{hi}-q}} dq \frac{A'_q q}{\xi^{-2} + q^2} \int_{E_{\text{min}}(q)}^{E'} \frac{dE}{E_{\text{den}}(q)}. \quad (2.18)$$

What is of more interest is the external yield

Y . We use the standard specular requirement that all electrons having energy associated with the direction normal to the surface sufficient to overcome the surface barrier, while retaining the energy parallel to the surface, will escape. Since for a given q , $E_{\text{min}}(q)$ is the energy associated with the z direction, we must have $E_{\text{min}}(q) + \hbar\omega > E_F + \Phi$, with Φ the work function. From Eqs. (2.11) and (2.13), we can write this as

$$E_{\text{min}} = (m/2q^2)(\omega - \hbar q^2/2m)^2 > E_F + \Phi - \hbar\omega.$$

So, in terms again of initial states,

$$Y = \begin{cases} 0, & \hbar\omega < \Phi; \\ \left(\int_{q_1}^{q_a} + \int_{q_b}^{q_{\text{hi}-q}} \right) dq \frac{A'_q q}{\xi^{-2} + q^2} \int_{E_{\text{min}}(q)}^{E'(q)} \frac{dE}{E_{\text{den}}}, & \Phi < \hbar\omega < E_F + \Phi; \\ Y', & \hbar\omega > E_F + \Phi; \end{cases} \quad (2.19)$$

$$q_a \left\{ = \left(\frac{2m}{\hbar^2} (E_F + \Phi) \right)^{1/2} \mp \left(\frac{2m}{\hbar^2} (E_F + \Phi - \hbar\omega) \right)^{1/2} \right. \quad (2.20)$$

The energy distributions dY'/dE and dY/dE for the dA/dz of Fig. 1 are given in Fig. 4. These

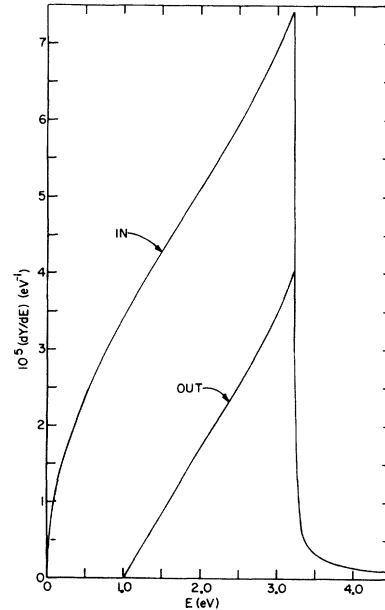


FIG. 4. Nonlocal energy distributions dY'/dE , denoted IN, and dY/dE , denoted OUT, for $\Omega = 0.75$, $\gamma = 10^{-2}$, $\theta_I = 45^\circ$, and $\Phi = 2.30$ eV. These calculations were made using an escape length $\xi = 10$ Å but the results are insensitive to this value (see text).

curves have been referred to the initial states so the peaks occur essentially at the Fermi energy. The high-energy tail resulting from damping is clearly evident.

We turn now to the angular distribution. Equation (2.18) can be converted to an angular distribution by recalling that the energy integral is over a plane of electrons of fixed k_z . If k_ρ is the wave vector in this plane [see Fig. 3(a)], the energy associated with this wave vector is $E_\rho^2 = \hbar^2 k_\rho^2 / 2m$ and dE_ρ [which is just dE in Eq. (2.18)] is $\hbar^2 k_\rho dk_\rho / m$. The angle θ_{in} (measured

from the surface normal) at which an excited electron from this plane is moving within the photoemitter is

$$\tan \theta_{in} = k_\rho / (k_z + q), \quad (2.21)$$

with k_z again the wave-vector component of the initial state. So,

$$dE_\rho = \hbar^2 (k_z + q)^2 \tan \theta_{in} \sec^2 \theta_{in} d\theta_{in} / m \quad (2.22)$$

and, since the distribution has azimuthal symmetry,

$$Y' = \frac{\hbar^2}{2\pi m} \int_{q_1}^{q_{hi-q}} dq \frac{A'_q q}{\xi^{-2} + q^2} \frac{(k_z + q)^2}{E_{den}(q)} \int_0^{\theta_{in}^{max}(q)} d\theta_{in} \int_0^{2\pi} d\phi \frac{\sin \theta_{in}}{\cos^3 \theta_{in}}, \quad (2.23)$$

where k_z is to be considered a function of q and

$$\tan \theta_{in}^{max}(q) = \{ (2m/\hbar^2) [E'(q) - E_{min}(q)] \}^{1/2} / [k_z(q) + q]. \quad (2.24)$$

To find the angular distribution outside the metal we must modify Eq. (2.21) to

$$\tan \theta_{out} = k_\rho / [(k_z + q)^2 - (2m/\hbar^2)(E_F + \Phi)]^{1/2} = k_\rho / [k_z^2 + (2m/\hbar^2)(\hbar\omega - E_F - \Phi)]^{1/2}, \quad (2.25)$$

so

$$Y = \begin{cases} 0, & \hbar\omega < \Phi; \\ \frac{\hbar^2}{2\pi m} \left(\int_{q_1}^{q_a} + \int_{q_b}^{q_{hi-q}} \right) dq \frac{A'_q q}{\xi^{-2} + q^2} \frac{(k_z + q)^2 - 2m(E_F + \Phi)/\hbar^2}{E_{den}(q)} \int_0^{\theta_{out}^{max}} d\theta_{out} \int_0^{2\pi} d\phi \frac{\sin \theta_{out}}{\cos^3 \theta_{out}}, & \Phi < \hbar\omega < E_F + \Phi; \end{cases} \quad (2.26)$$

with

$$\tan \theta_{out}^{max}(q) = \left(\frac{2m[E'(q) - E_{min}(q)]/\hbar^2}{(k_z + q)^2 - 2m(E_F + \Phi)/\hbar^2} \right)^{1/2}. \quad (2.27)$$

For $\hbar\omega > E_F + \Phi$, Y is the same as for $\Phi < \hbar\omega < E_F + \Phi$ except the q integral is from q_1 to q_{hi-q} .

Several angular distribution curves for the conditions used in this section are given in Fig. 5. The curve labeled $dY/d\theta|_{in}$ is $dY'/d\theta_{in}$ obtained from Eq. (2.23) after integrating over $d\phi$ and represents the angular distribution of excited electrons within the metal; specifically, $(dY/d\theta|_{in}) d\theta_{in}$ is the yield into a ring of polar angle spread $d\theta$ ($d\theta$ in degrees). The curve $dY/d\Omega|_{in}$ is $dY'/d\Omega_{in}$ from Eq. (2.23), the distribution inside the metal per unit solid angle with $d\phi$ in radians and $d\theta_{in}$ in degrees. These quantities are related by $dY/d\theta|_{in} = 2\pi \sin\theta (dY/d\Omega|_{in})$. For small angles we see the interesting effects of damping. The primary role of damping is to push a small bulge of electrons out from the neighborhood of the point P_1 in Fig. 3(a), the lemon effect alluded to earlier. This is just another way of expressing the spreading of the single-particle region and, for the last time, we emphasize that this is a final-state effect which appears here as a Fermi-

surface distortion only because we are referring the final states back to the initial states. The electrons in the bulge are all moving essentially normal to the surface and contribute the striking small-angle structure. The fact that $dY/d\Omega|_{in}$ is essentially constant for $\theta \lesssim 2^\circ$ is a consequence of using the minimum in A'_q (Fig. 2) as the lower limit of the q integration, that is, A'_q is finite at the lower limit. If we had treated the damping-induced transverse spread of the electrons more carefully, we would expect the small-angle peak to be reduced somewhat in size and broadened. Since $k_z + q$ can also be written

$$k_z + q = (k_z^2 + 2m\omega/\hbar^2)^{1/2}, \quad (2.28)$$

we see from Eq. (2.24) that the maximum internal angle for an excited electron results from an initial state on the Fermi surface with $k_z = 0$. For such an electron, $k_\rho = (2mE_F/\hbar^2)^{1/2}$ and $q = (2m\omega/\hbar^2)^{1/2}$. Thus the maximum internal angle is $\tan^{-1}(E_F/\hbar\omega)^{1/2} = 40.2^\circ$ consistent with Fig. 5.

External to the metal, the angular distribution

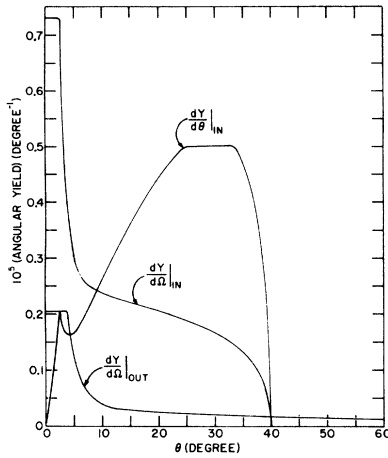


FIG. 5. Nonlocal angular distributions for $\Omega = 0.75$, $\gamma = 10^{-2}$, and $\theta_T = 45^\circ$. $dY/d\theta|_{in}$ is the internal distribution per unit polar angle, $dY/d\Omega|_{in}$ the internal distribution per unit solid angle, and $dY/d\Omega|_{out}$ the external distribution per unit solid angle.

is obtained from Eq. (2.26) and is shown as the curve labeled $dY/d\Omega|_{out}$ in Fig. 5. As a result of the diffraction at the surface, the low-angle peak due to the damping has spread out. Since $\hbar\omega < E_F + \Phi$, the total external yield is well below the internal and the external angular distribution extends to 90° .

Another distribution of interest is the energy-analyzed angular distribution. Think of an energy-analyzing ring detector with the axis normal to the surface and having a polar-angle width $\Delta\theta$. For the internal electrons, the corresponding distribution can be found from Eq. (2.23) by doing the ϕ integral and integrating $d\theta$ over the desired range $\Delta\theta$ while recognizing that for a given q there is a unique relation between the energy of an electron and the polar angle describing its direction of motion. The internal energy distribution curves for a ring with $\Delta\theta = 1^\circ$ situated at various polar angles is shown in Fig. 6, again referred to initial states. We see here some remarkable curves. For a given angle, there is a low-energy cutoff followed by a very sharp peak and then a tailing off. The fact that damping effects in our model are concentrated near small angles is indicated by the fact that the curves labeled 1 and 7 (corresponding to θ from 0 to 1° and 6 to 7° , respectively) extend beyond the Fermi energy while curves for larger angles drop off near the Fermi energy. The occurrence of the peaks can be understood by examining the special group of electrons which appears at a given angle. Using Eqs. (2.21) and (2.28), the relationship between θ_{in} and the wave vector components of

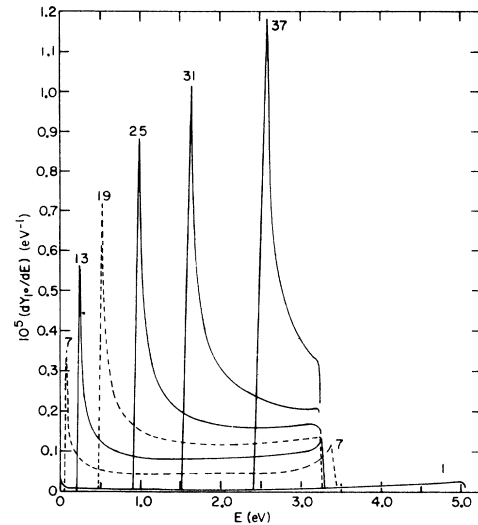


FIG. 6. Energy distribution curves for the internal yield into a ring of polar-angle width 1° for $\Omega = 0.75$, $\gamma = 10^{-2}$, and $\theta_T = 45^\circ$. If the number shown on a curve is s , the angular range is $(s-1)$ to s° .

the initial state, k_x and k_ρ , is

$$\tan\theta_{in} = k_\rho / (k_x^2 + 2m\omega/\hbar)^{1/2}. \quad (2.29)$$

By taking θ_{in} as fixed, this expression yields a "trajectory" in the k_ρ - k_x plane, and it is the electrons along this trajectory which contribute to the yield at θ_{in} . Examples of these hyperbolic trajectories for the conditions of the present section are shown in Fig. 7(b). Taking the 24° - 25° range as an example, the low-energy cutoff would occur at $k_x = 0$ and $\theta = 24^\circ$, or 0.903 eV. The large peaks occur at the large density of states where the trajectories go vertically through the k_ρ axis. For the 24° - 25° case, the peak will then occur for $k_x = 0$ and $\theta \approx 25^\circ$ or an energy of about 0.99 eV. These features are confirmed in Fig. 6.

It should be noted that damping is not properly represented in Fig. 6. Our damping model was designed to provide a description of the rearrangement of the outer Fermi-sphere electrons due to damping, but did not entail the assignment of a width to the individual states. These two possibilities are essentially equivalent for the outer electrons, but the former leaves the inner states unbroadened as they were without damping. Since the peaks in Fig. 6 come from initial electrons far from the Fermi surface, they have not been broadened so the peaks should be somewhat wider than shown and the low-energy cutoff will not be abrupt.

Suppose we now go outside the metal. Interestingly, the large peaks in Fig. 6 vanish since we have here the condition $\hbar\omega < E_F + \Phi$. This means

that those initial states which cannot contribute external electrons include the k_z range

$$|k_z| < [2m(E_F + \Phi - \hbar\omega)/\hbar^2]^{1/2},$$

and it is the region near $k_z=0$ which gives rise to the peaks in Fig. 6. This remarkable difference in the character of the fixed-angle distributions, inside and outside, when $\hbar\omega < E_F + \Phi$ appears in the equations determining the trajectories:

$$k_\rho^2/\tan^2\theta_{in} - k_z^2 = 2m\omega/\hbar \quad (\text{inside}),$$

$$k_z^2 - k_\rho^2/\tan^2\theta_{out} = (2m/\hbar^2)(E_F + \Phi - \hbar\omega) \quad (\text{outside}),$$

with k_z and k_ρ those of the initial states. Inside, the axis of the hyperbola is the k_ρ axis while outside it is the k_z axis. Inside, the hyperbola crosses the k_z axis at $k_\rho^2 = (2m\omega/\hbar)\tan^2\theta_{in}$, while outside the hyperbola crosses the k_ρ axis at $k_z^2 = (2m/\hbar^2)(E_F + \Phi - \hbar\omega)$ which is independent of θ_{out} . If ds is the length element along the trajectories, the density of initial energy states on a trajectory, $dn/dE \propto ds/dE$. Since the geometrical figure which determines the yield involves rotation about the k_z axis, the relevant quantity is $G \equiv k_\rho(ds/dE)$. Inside, we have

$$G_{in} \propto \tan\theta_{in} \left(\frac{E \cos^2\theta_{in} + \hbar\omega(\cos^2\theta_{in} - \sin^2\theta_{in})}{E - \hbar\omega \tan^2\theta_{in}} \right)^{1/2}. \quad (2.30)$$

Since G_{in} must be real, $E \geq \hbar\omega \tan^2\theta_{in}$. The sharp peaks in Fig. 6 are associated with this lower limit where $G_{in} \rightarrow \infty$. We also find: outside and $\hbar\omega < E_F + \Phi$

$$G_{out} = G_{in},$$

with

$$\hbar\omega \rightarrow \hbar\omega - E_F - \Phi \quad \text{and} \quad E > E_F + \Phi - \hbar\omega.$$

For all external angles, these distributions will be approximately triangular and extend from $E = E_F + \Phi - \hbar\omega$ to roughly the Fermi energy or somewhat beyond, if θ_{out} is small, because of damping. In addition: outside and $\hbar\omega > E_F + \Phi$

$$G_{out} = G_{in},$$

with

$$\hbar\omega \rightarrow \hbar\omega - E_F - \Phi.$$

Thus, sharp peaks like those in Fig. 6 will appear in the external yield when $\hbar\omega > E_F + \Phi$. Equations (2.30)–(2.32) should only be used in a qualitative way. These trajectories involve a range of q values and in the photoyield the various parts of the trajectory will be weighted by the appropriate A'_q . This has not been included; to do so would entail multiplying the G 's by nonsingular functions

of q and θ .

We conclude this section with a few comments about the final states even though we will continue to refer the yield to the initial states. A sketch of the nonlocal excited states for the direction of q indicated and $\hbar\omega = 2E_F$ is given in Fig. 7(a). The plane underlying the spherical segment of excited states results from excitation of the initial-state, $k_z=0$ electron plane. All other initial states, $-k_F < k_z < k_F$, give rise to excited states with larger final state k_z 's.

Figure 7(a) also indicates why our treatment above must be modified when $\hbar\omega < E_F$. Under this condition, the excited-state spectrum has a spherical segment cut out of the bottom due to the Pauli principle. This means that only some of the initial states of the Fermi sphere can contribute to the yield and, for example, $E_{min}(q)$ as well as $E_{den}(q)$ in Eq. (2.18) differ from those used above. In practice, this makes very little difference since it only affects the theory for $\Phi < \hbar\omega < E_F$, and then only for initial states with $E \leq E_F - \hbar\omega$, states where A'_q is well below its maximum.

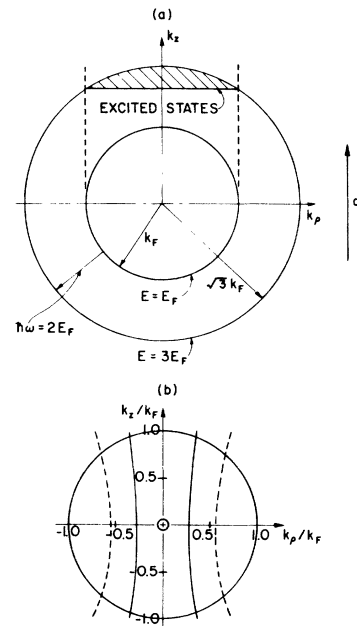


FIG. 7. (a) Nonlocal excited-state spectrum for $\hbar\omega = 2E_F$ and no damping. The excited states for momentum transfer q in the k_z direction is the crosshatched region which is the cross section of a spherical segment. (b) "Trajectories" of initial states contributing to the internal yield for $\Omega = 0.75$ with momentum transfer in the k_x direction. The curves shown are for an arbitrary plane containing the k_z axis so in three dimensions the trajectories become hyperboloids of revolution. Solid line: $\theta_{in} = 13^\circ$; dashed line: $\theta_{in} = 25^\circ$.

III. RESULTS AND DISCUSSION

We now wish to expand the discussion of Sec. II to include a wide frequency range. Before doing this, we point out that the theory above for the nonlocal yield bears a striking resemblance to the theory for the photoyield resulting from inter-band transitions as developed by Mahan.⁸ If we consider a single slab of initial-state electrons of given k_x , the associated q plays much the same role in the present theory as the reciprocal-lattice vector \vec{G} plays in the "primary cone" contribution to the yield in Mahan's theory. The principal differences are that here we have a continuous range of q values that must be considered and our q is always normal to the surface.

Since we have taken the work function to be 2.30 eV, the photoemission cutoff occurs at $\Omega = 0.379$. For frequencies from this low-energy cutoff to $\hbar\omega = E_F + \Phi$, $\Omega = 0.916$, the results are qualitatively as described above for $\Omega = 0.75$. Details depend upon Ω , γ , and θ_I , but not ξ since ξ is probably ≈ 20 Å in this energy range. There will occur a maximum in the yield for given θ_I in the range $0.6 \lesssim \Omega \lesssim 0.8$, the exact value depending upon θ_I . Peaks in the energy-resolved angular distributions such as those in Fig. 6 will not appear in the external yield until $\Omega > 0.916$ as discussed above.

As the frequency increases toward the plasma frequency, the nonlocal yield is strongly reduced because the total electric field is strongly suppressed in the surface region.^{2,4} We illustrate the significant extent of this suppression in Fig. 8. For $\Omega = 0.99$ and $\gamma = 10^{-2}$, the nonlocal dA/dz is an apparently smooth curve starting, of course, from zero at $z = 0$. Note that the nonlocal dA/dz does not reach the level of the local result until $z \sim 28$ Å. Not only is there no evidence of the nonlocal oscillations, but the local yield will also be strongly suppressed for $\xi \lesssim 20$ Å. To show that there remains a small nonlocal contribution hidden in dA/dz , we calculated dA/dz with γ reduced to 10^{-4} . This result, multiplied by 100, is shown in Fig. 8 and exhibits the nonlocal oscillations, though they are small by comparison with those of Fig. 1. A calculation of A'_q gives a curve which looks much like that of Fig. 2 but the maximum A'_q in the single-particle region is, on the same scale used in Fig. 2, only 0.15 or more than 100 times smaller than the maximum value in Fig. 2. Keeping γ at 10^{-4} but increasing Ω to 0.999, we see in Fig. 8 that the suppression of the surface-region electric field keeps the nonlocal dA/dz below that given by the local expression to a distance of about 60 Å into the metal and the nonlocal oscillations are barely visible.

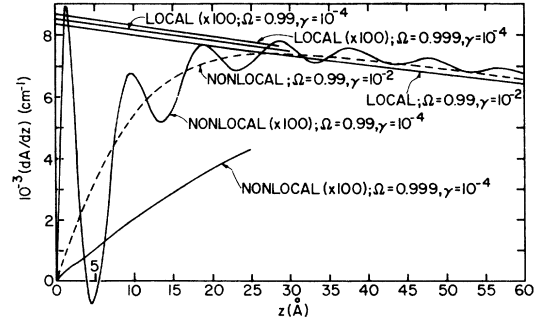


FIG. 8. Distribution of absorbed energy dA/dz for $\Omega = 0.99$, $\gamma = 10^{-2}$, $\theta_I = 45^\circ$, for $\Omega = 0.99$, $\gamma = 10^{-4}$, $\theta_I = 45^\circ$ (shown multiplied by 100), and for $\Omega = 0.999$, $\gamma = 10^{-4}$, $\theta_I = 45^\circ$ (shown multiplied by 100). Local values calculated as described in Table I are also given.

It is important to understand the nature of the nonlocal dA/dz in Fig. 8. The nonlocal oscillations, due to the single-particle excitations and involving large q , are superposed upon a local or small- q curve, but this local curve is vastly different from the local curve resulting from a purely local theory. An expression for the local part of the nonlocal curves of Fig. 8 can be obtained using the procedure given in Ref. 2. This procedure involves using the small- q approximation to the longitudinal dielectric function, appropriate for the local part. This approximation leads to the "local" expression for the electric field component E_x given as Eq. (3.6) in Ref. 2. Evaluating $J_x(q)$ in the same approximation and then forming

$$\frac{dA}{dz} = \frac{4\pi}{c \cos \theta_I} \operatorname{Re}(J_x E_x^*)$$

yields

$$\left. \frac{dA}{dz} \right|_{\text{local}} = \alpha A_x \left[e^{-\alpha z} - e^{-q'_s z} e^{-\xi'' z} \times \left(\cos(q'_s - \xi')z + \frac{\epsilon'}{\epsilon''} \sin(q'_s - \xi')z \right) \right], \quad (3.1)$$

where α is given by (2.6), $\epsilon = \epsilon' + i\epsilon''$ by (2.7),

$$\xi = \xi' + i\xi'' = \frac{\omega}{c} (\epsilon - \sin^2 \theta_I)^{1/2}, \quad (3.2)$$

$$q'_s = (q'_s + iq''_s)^2 = (5/3v_F^2) \{ \omega_p^2 \Omega^2 [\Omega(\Omega + i\gamma) - 1] \}, \quad (3.3)$$

and A_x , that part of the local absorptance associated with the z direction, by

$$A_x = \frac{4\omega_p \Omega \epsilon''}{c\alpha} \frac{\sin^2 \theta_I \cos \theta_I}{|\epsilon \cos \theta_I + (\epsilon - \sin^2 \theta_I)^{1/2}|^2}. \quad (3.4)$$

This function describes well the local parts of

the nonlocal curves in Fig. 8. It is necessary to use expression (3.1) to describe the local part of dA/dz for $0.9 \leq \Omega \leq 1.0$. For frequencies below 0.9, q_s'' becomes large and the local part of dA/dz is, except for very small z , the usual local value (see Fig. 1).

For frequencies above the plasma frequency, an additional nonlocal contribution to dA/dz appears, that due to the plasmon. This is clearly indicated in Eq. (3.1) since, as Ω increases beyond 1, q_s changes from essentially imaginary to essentially real and q_s' is just the wave vector of the plasmon in the low- q approximation. The second term in (3.1) is then the oscillatory term due to the plasmon. Since the plasmon damping represented by q_s'' will usually be considerably larger than α , it is appropriate to view (3.1) as the plasmon oscillations superposed upon the slowly decaying local contribution. Thus for $\Omega \geq 1 + \gamma$, it is a reasonable approximation to take for the local contribution the usual local expression which is just the first term of Eq. (3.1).

Below the plasma frequency, it is the single-particle excitations, not included in (3.1), which give rise to the nonlocal photoyield. When the frequency is above the plasma frequency, these single-particle excitations do not change their character in any important way. Thus, independent of the plasmon, we expect a nonlocal yield for $\Omega > 1$ and can see no reason for the claim of Feibelman³ that the nonlocal yield should die out above $\Omega = 1$. Indeed, we find results in marked contrast to his.

Consider now $\Omega = 1.2$ with $\gamma = 10^{-2}$ and $\theta_I = 45^\circ$. The curve of dA/dz for these conditions is much like that of the curve labeled $\Omega = 1.155$, $\theta = 30^\circ$ in Fig. 2 of Ref. 1, that is, a sinusoid exhibiting essentially no decay with increasing distance.⁹ That this should be the case is clear from Fig. 9 which shows the Fourier transform A'_q dominated by the large narrow plasmon peak. Since we are at a frequency below that at which Landau damping sets in, that is, the frequency Ω_L where the plasmon dispersion curve enters the single-particle region ($\Omega_L = 1.48$ for the electron density used here), the width of the plasmon is due essentially only to the finite value of γ and thus the standing plasmon wave in dA/dz extends hundreds of angstroms into the metal. Above the plasmon peak in Fig. 9 is the contribution from the single-particle region, which, because of the large plasmon peak, appears small but is in fact considerably larger than that of Fig. 2.

As we discussed at length in Ref. 2, the plasmon can contribute to the photoyield only to the extent that it decays into single-particle excitations, a process which is in detail unique for each metal

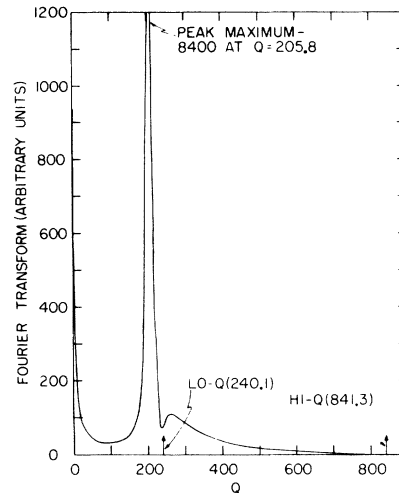


FIG. 9. Fourier transform A'_q of dA/dz for $\Omega = 1.2$, $\gamma = 10^{-2}$, and $\theta_I = 45^\circ$. The units of A'_q are arbitrary but the same as those in Fig. 2.

since it depends upon the details of the band structure. Let us here consider only the yield due to the single-particle region; we will return to this point below.

From Fig. 9 we see that there is no clear division between the upper- q part of the plasmon peak and the single-particle region. This means, of course, that the plasmon extends into the single-particle region and so, even in this case where $\Omega < \Omega_L$, the plasmon contributes to the yield from the single-particle region.¹⁰ The single-particle yield has here been calculated using the minimum

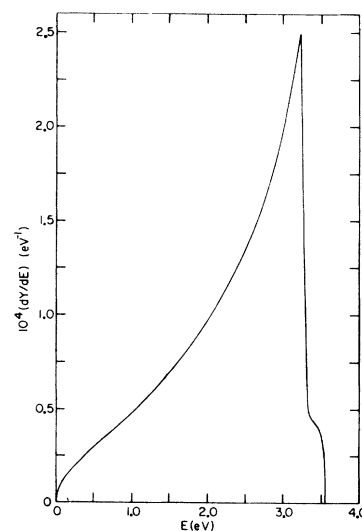


FIG. 10. Nonlocal energy distribution dY/dE for $\Omega = 1.2$, $\gamma = 10^{-2}$, and $\theta_I = 45^\circ$. Since $\Omega > (E_F + \Phi) \cong 0.92$, this curve is the same within and without the metal.

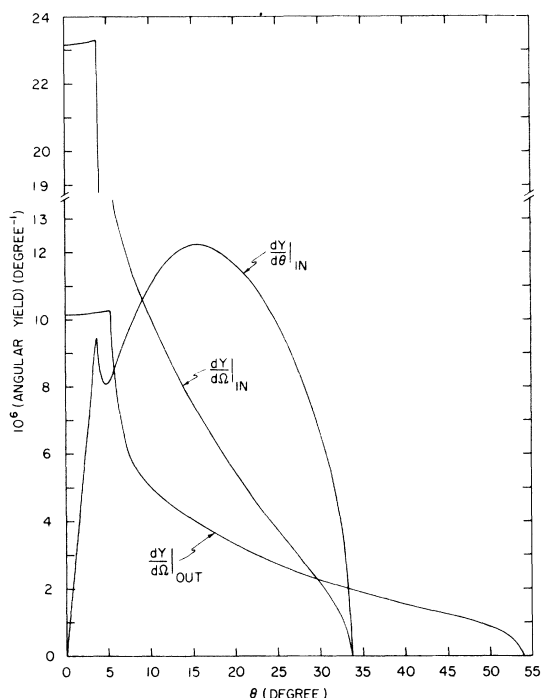


FIG. 11. Nonlocal angular distributions for $\Omega = 1.2$, $\gamma = 10^{-2}$, $\theta_f = 45^\circ$, and $\Phi = 2.30$ eV. See caption of Fig. 5 for definitions.

in A'_q below the low- q edge as q_1 . The resulting energy distribution is shown in Fig. 10. As a result of the plasmon contribution coming in at the low- q edge of the single-particle region, the contribution to dY/dE at high energies is enhanced and dY/dE is concave upwards. It is the fact of cutting off the q integration abruptly that gives the strange high-energy cutoff in dY/dE . In the angular distribution (Fig. 11) the cutoff in the q integral gives rise to the extended, roughly flat-topped regions at low angles. If we had extended the q integral to lower values with a smooth extrapolation of A'_q to zero, the high-energy tail in Fig. 10 would be extended and the low-angle peaks in Fig. 11 would extend upward and not be flat topped. We note that both internal and external angular distributions have contracted significantly in angular spread from those of Fig. 5. Internal energy-resolved yields for a 1° polar angle spread are qualitatively like those of Fig. 6 and now these peaks also occur in the external yield. In addition, the peaks in the 1° yields near the Fermi energy are more prominent for small angles because of the larger A'_q values near the low- q edge of the single-particle region.

As was indicated above, the frequency Ω_L at which Landau damping sets in is $\Omega_L = 1.48$ for the present conditions. For frequencies larger than

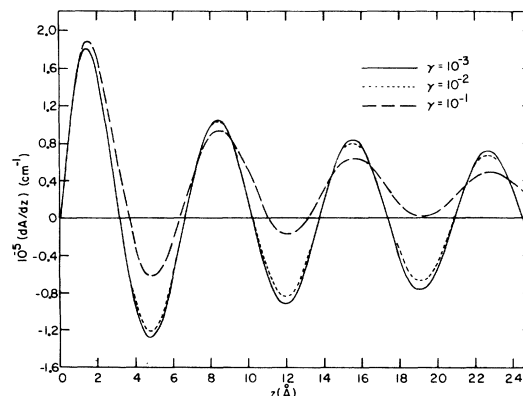


FIG. 12. Distribution of absorbed energy dA/dz for $\Omega = 1.50$, $\theta_f = 75^\circ$, and various values of γ . Local values are given in Table I.

Ω_L the plasmon will be situated more or less completely within the single-particle region and thus can decay into single-particle excitations. For $\Omega = 1.50$, dA/dz is given in Fig. 12. Damping of the oscillations is considerable, even for $\gamma = 10^{-3}$, consistent with the location of the plasmon. The Fourier transform A'_q is shown in Fig. 13 and, as expected, the plasmon peak is sharply reduced in magnitude from that of Fig. 9. Because the plasmon is located just inside the low-

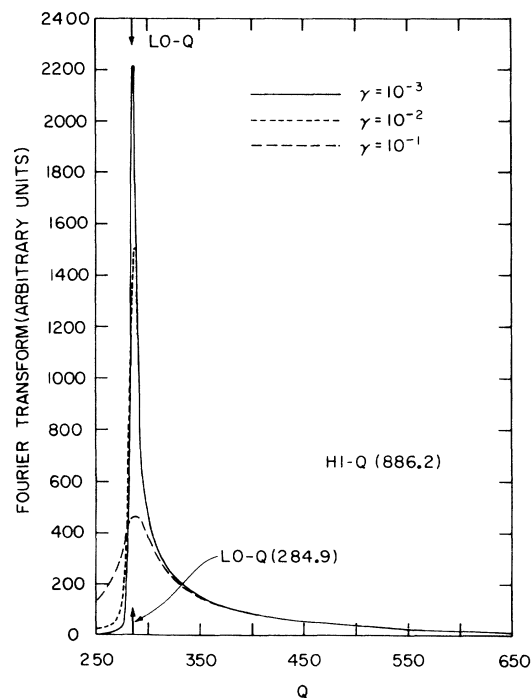


FIG. 13. Fourier transform A'_q of dA/dz for $\Omega = 1.50$, $\theta_f = 75^\circ$, and various values of γ . The units of A'_q are arbitrary but the same as those in Figs. 2 and 9.

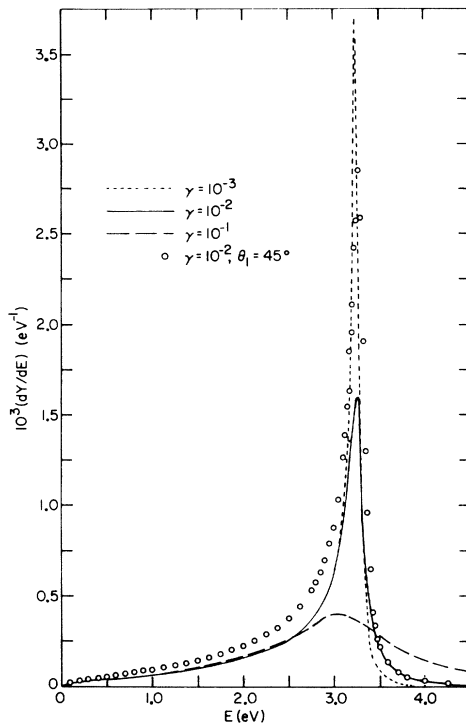


FIG. 14. Nonlocal energy distributions dY/dE for $\Omega = 1.50$, $\theta_f = 75^\circ$, and various values of γ are given by the several lines. dY/dE for $\Omega = 1.50$, $\theta_f = 45^\circ$, and $\gamma = 10^{-2}$ is shown by the circles.

q edge of the single-particle region, dY/dE will be strongly peaked near the Fermi energy if the damping is not too large; this is shown in Fig. 14. When γ is as large as 10^{-1} , our treatment of damping leads to a large high-energy tail due to the now markedly spread single-particle region and the location of the plasmon. Angular distributions for $\gamma = 10^{-2}$ are given in Fig. 15. Increasing γ reduces in magnitude and broadens the low-angle structure while decreasing γ compresses the peaks and increases their magnitude sharply. The concentration of the angular yield to small angles influences strongly the 1° yields as indicated in Fig. 16. For low angles, the combination of the damping and the plasmon near the low- q edge enhances the "lemon effect" and this shows up clearly in the 1° yields for $\theta \lesssim 13^\circ$. Keep in mind that the energies at which the low-energy peaks appear will differ outside the metal.

Increasing Ω to 1.6, thereby moving the plasmon more firmly into the single-particle region and enhancing its decay into single-particle excitations, produces only expected changes in the various yields for $\Omega = 1.5$. The plasmon peak in the Fourier transform A'_q is broadened and reduced (by ~ 2 from that of Fig. 13 for $\gamma = 10^{-3}$). As a result,

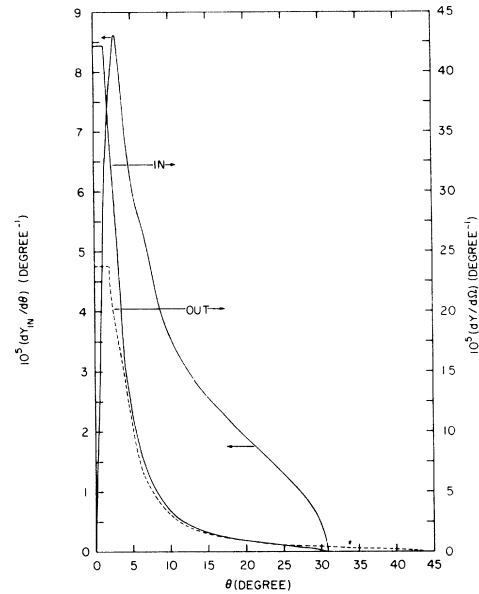


FIG. 15. Nonlocal angular distributions for $\Omega = 1.5$, $\gamma = 10^{-2}$, $\theta_f = 75^\circ$, and $\Phi = 2.30$ eV. See caption of Fig. 5 for definitions.

the peaks in dY/dE near E_F are reduced but, for low damping, the curves remain strongly concave upwards. Also, the low-angle peaks in the angular yields are reduced in magnitude and the

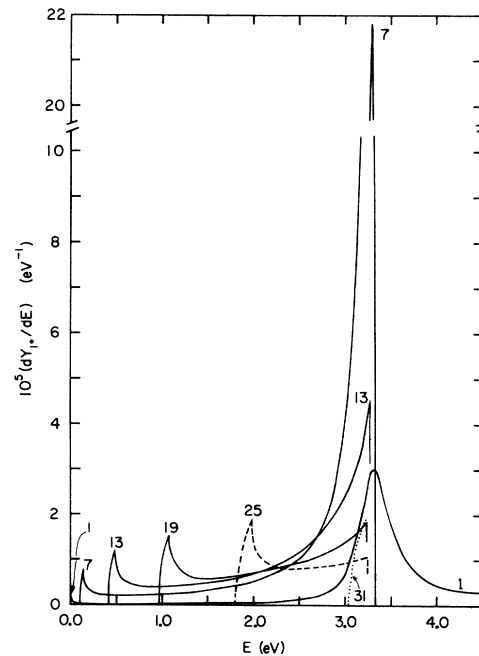


FIG. 16. Energy distribution curves for the internal yield into a ring of polar-angle width 1° for $\Omega = 1.5$, $\gamma = 10^{-2}$, and $\theta_f = 75^\circ$. If the number shown on a curve is s , the angular range is $(s-1)$ to s° .

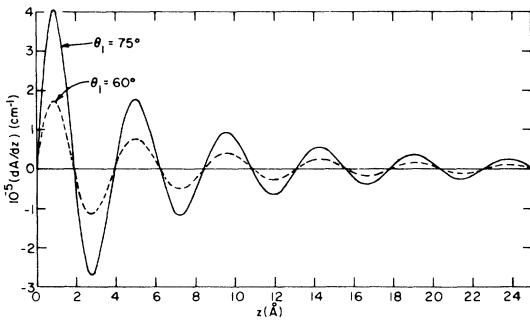


FIG. 17. Distribution of absorbed energy dA/dz for $\Omega = 2.5$, $\gamma = 10^{-2}$, and two angles of incidence, θ_i equals 60° and 75° . The parameters describing the local expression are given in Table I.

contributions to the 1° yields near the Fermi energy for small angles is reduced.

As Ω increases further the plasmon continues to recede into the single-particle region and becomes essentially an indistinguishable part thereof. As this happens, the picture returns to a form qualitatively much like that for $\Omega = 0.75$. We illustrate for $\Omega = 2.5$ and $\gamma = 10^{-2}$. Curves of dA/dz shown in Fig. 17 exhibit rapid damping of the oscillations and the resulting Fourier transforms (Fig. 18) possess the same features as that of Fig. 2. The energy distributions dY/dE are again roughly triangular (Fig. 19) and both the angular distributions (Fig. 20) and the 1° yields (Fig. 21) look much as they did for $\Omega = 0.75$ (Figs. 5 and 6). Note, however, that the magnitudes of all the yields are much greater than they were at $\Omega = 0.75$.

We now wish to make some addition comments on the total nonlocal yield and the role of the plasmon, referring to Fig. 22 which shows the frequency dependence of the yield. Consider $\theta_i = 45^\circ$ and keep in mind that we are here considering only the nonlocal part of the yield associated with the z components of \vec{J} and \vec{E} . For $\Omega \lesssim 0.92$, the internal yield is reduced externally by the surface barrier. As $\Omega \rightarrow 1$ from below, the reduction

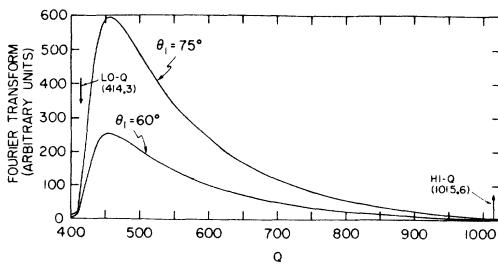


FIG. 18. Fourier transform A'_q of dA/dz for $\Omega = 2.5$, $\gamma = 10^{-2}$, and two angles of incidence, θ_i equals 60° and 75° . The units of A'_q are arbitrary, but the same as those in Figs. 2, 9, and 13.

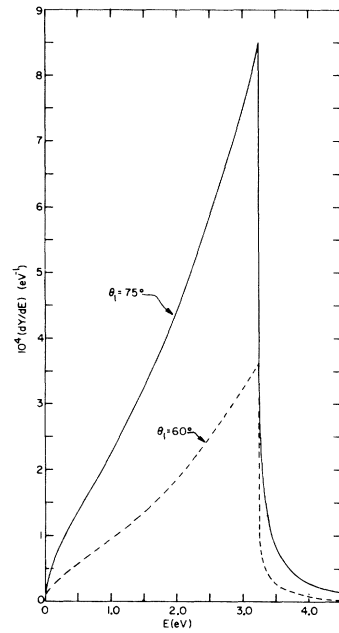


FIG. 19. Nonlocal energy distributions dY/dE for $\Omega = 2.5$, $\gamma = 10^{-2}$, and two angles of incidence, $\theta_i = 60^\circ$ and 75° .

of the surface-region electric field essentially eliminates the yield. As Ω increases beyond one, the plasmon enters the picture. Above we considered only the yield associated with the single-

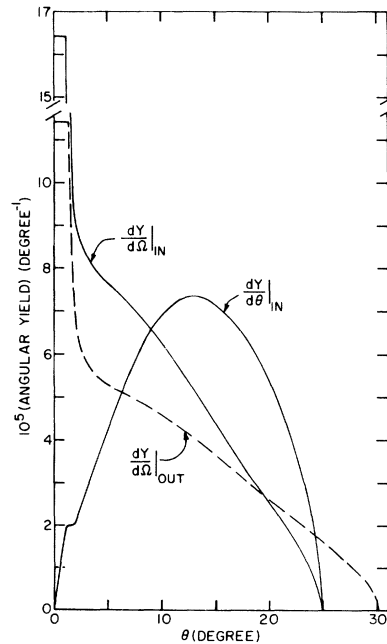


FIG. 20. Nonlocal angular distributions for $\Omega = 2.5$, $\gamma = 10^{-2}$, $\theta_i = 75^\circ$, and $\Phi = 2.30$ eV. See caption of Fig. 5 for definitions.

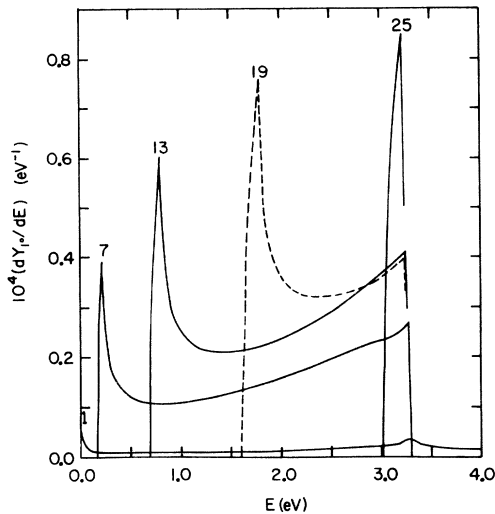


FIG. 21. Energy distribution curves for the internal yield into a ring of polar-angle width 1° for $\Omega = 2.5$, $\gamma = 10^{-2}$, and $\theta_I = 75^\circ$. If the number shown on a curve is s , the angular range is $(s - 1)$ to s° .

particle region, which means, of course, that the plasmon contributes substantially only for $\Omega \approx \Omega_L = 1.48$. The curve underlying the $\theta_I = 45^\circ$ crosshatched region is the single-particle-region yield. If we simply include the plasmon in the total yield by extending the q integration in Eq. (2.19) to include the plasmon peak in A'_q (without specifying a mechanism by which the plasmon can produce photoelectrons) we obtain the yield curve given by the upper boundary of the crosshatched region. Depending upon the system, that is, the extent to which the plasmon decays into excited electrons which can escape, the yield could then range throughout the crosshatched region.

Yields versus frequency curves for the case where the plasmon is included have been given in Ref. 2. It should be noted that our electron gas model does not provide a mechanism for plasmon decay when $\Omega \lesssim \Omega_L$. So, while we can formally incorporate the plasmon into the total yield, we cannot describe the effects of the plasmon on the energy and angular distributions.

Let us examine the limit where the plasmon contributes essentially no photoelectrons for $\Omega \lesssim \Omega_L$. The character of the photoyield can then be rather complicated. The peak in the 45° yield of Fig. 22, with the plasmon included, is an optical effect² and occurs when the local dielectric function $\epsilon(\omega) \approx \sin^2 \theta_I$ or, for the electron gas, $\Omega \approx (\cos \theta_I)^{-1}$. So, when $\theta_I \lesssim 30^\circ$, the single-particle photoyield would have a small maximum for $\Omega \lesssim 1.15$ and would then decrease until $\Omega \sim \Omega_L$ where it would increase sharply. For $30^\circ \lesssim \theta_I$

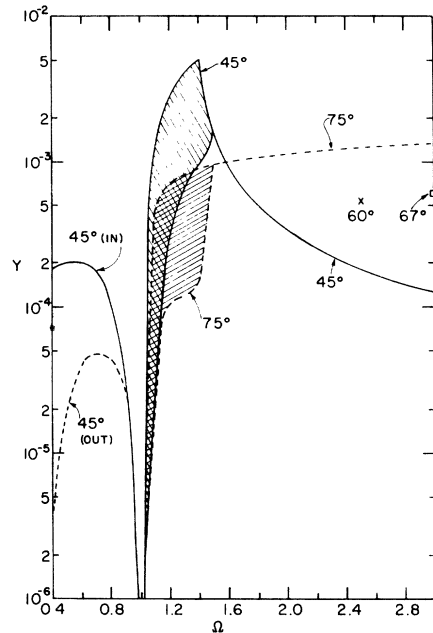


FIG. 22. Total yields as a function of frequency Ω for $\gamma = 10^{-2}$. The angle of incidence is given on the curves. For $\theta_I = 45^\circ$, both the internal and external yields are shown for the entire frequency range of the figure. The curve underlying the crosshatched region is the yield from only the single-particle excitations and the curve defining the top of the crosshatched region is the yield with the plasmon included for $1 < \Omega < 1.48$. Yields for $\theta_I = 75^\circ$ are given only for $\Omega > 1$ with the borders of the crosshatched region defined as for $\theta_I = 45^\circ$. Two points for $\theta_I = 60^\circ$ and 67° are also shown. These curves are essentially independent of the escape length ξ if $\xi \gtrsim 3 \text{ \AA}$ except in the range $1 < \Omega < 1.48$ when the plasmon is included. Then we used $\xi = 10 \text{ \AA}$.

$\lesssim 47.5^\circ$ [$47.5^\circ = \cos^{-1}(1/\Omega_L)$], these peaks would merge with the sharp rise at Ω_L dominating; this is the case for $\theta_I = 45^\circ$ in Fig. 22. For $\theta_I > 47.5^\circ$, the single-particle yield would increase from $\Omega = 1$ and then increase sharply for $\Omega \sim \Omega_L$. This is shown for $\theta_I = 75^\circ$ in Fig. 22 where the top of the crosshatched region is again the yield with the plasmon included and the bottom, that due only to the single-particle region. The extent of the yield increase for $\Omega \sim \Omega_L$ is better indicated by the $\theta_I = 75^\circ$ curve as the obscuring effects of the optics are removed. So, the most dramatic manifestation of the plasmon when it is weakly damped and contributes but little to the yield for $\Omega < \Omega_L$ (probably the normal case) is to increase the yield strikingly for $\Omega \sim \Omega_L$.

IV. SUMMARY AND CONCLUSIONS

A detailed description has been given of the nonlocal surface photoyield resulting from the

normal component of the electric field for an electron gas excited by p -polarized light. These yields are not insignificant, indicating that the basic physical fact leading to their existence, a strong dependence of the electric field (or the vector potential) on distance from the surface must be allowed for in general.

For an actual metal, our detailed description will of course be modified by the addition of bulk contributions such as those from interband transitions. However, within the total photoyield, comprised of the bulk contribution and the non-local or surface yield, features of the latter, as described by the present theory, should be manifested. These include: (i) surface contributions to the energy distribution curves strongly peaked near the Fermi energy; (ii) surface contributions to the angular distributions of the yield, which are confined to a decreasing angular range with increasing light frequency; (iii) unique and unexpected structure in the energy-resolved angular distributions; (iv) a reduction of the total p -polar-

ized yield for $\Omega \approx 1$ [more generally, $\epsilon(\omega) \approx 0$]; and (v) structure due to the plasmons. For $\Omega \sim 2-3$, the electron escape lengths ξ are very small.^{11,12} Under these conditions, the surface yield, essentially independent of ξ , might dominate the total yield.

The photoemission discussion presented herein does not represent a complete description within the model used. We have not included yield contributions associated with the electric field component parallel to the surface nor contributions resulting from local effects associated with the normal component of the electric field. In our previous work we have implied that the former can be considered local, but we now know this to be not the case.¹³ A proper treatment of the photoyield resulting from the local part of the optical absorption means, in our model, a theory for the photoyield due to the Drude absorption. This is of general interest for photoemission due to moderate-energy light and will be reported shortly.¹⁴

*Work performed for the U. S. Energy Research and Development Administration under Contract No. W-7405-eng-82.

¹K. L. Kliewer, Phys. Rev. Lett. **33**, 900 (1974).

²K. L. Kliewer, Phys. Rev. B **14**, 1412 (1976).

³P. Feibelman, Phys. Rev. Lett. **34**, 1092 (1975).

⁴J. G. Endriz, Phys. Rev. B **7**, 3464 (1973).

⁵J. K. Sass, H. Laucht, and K. L. Kliewer, Phys. Rev. Lett. **35**, 1461 (1975).

⁶R. Fuchs and K. L. Kliewer, Phys. Rev. **185**, 905 (1969).

⁷N. D. Mermin, Phys. Rev. B **1**, 2362 (1970).

⁸G. D. Mahan, Phys. Rev. B **2**, 4334 (1970).

⁹These are just the oscillations that give rise to the

plasmon resonances in thin metal films. See A. R. Melnyk and M. J. Harrison, Phys. Rev. Lett. **21**, 85 (1969); and Ref. 6.

¹⁰In contrast to the single-particle effects, the nonlocal plasmon behavior is strongly dependent upon damping, and thus the extent to which the plasmon extends into the single-particle region depends strongly on γ . We will examine this point below.

¹¹C. R. Brundle, J. Vac. Sci. Technol. **11**, 212 (1974).

¹²C. J. Powell, Surf. Sci. **44**, 29 (1974).

¹³K. L. Kliewer, P. Rimbey, and R. Fuchs (unpublished).

¹⁴K. L. Kliewer and K. H. Bennemann, Phys. Rev. (to be published).